Method for Determining Optimum Operational Conditions of Microbubble Scrubber Using Image Processing

Y. Yoo[1, 2], H. Park[1, 2], Y. Choi[1, 2], J. Jung[3], H. Song[1], J. Kim[1, *], and H. Cho[1, *]

[1] *Green Materials and Processes R&D Group, Korea Institute of Industrial Technology, 55 Jonga-ro, Ulsan 44413, Republic of Korea*
[2] *Department of Chemical and Biomolecular Engineering, Yonsei University, 50 Yonsei-ro, Seoul 03722, Republic of Korea*
[3] *Hankook Engineering Co., Ltd, 252 Gokcheon geomdan-ro, Ulsan 44965, Republic of Korea*

ABSTRACT. This paper presents an image-processing-based model for calculating the interfacial-area concentration (IAC) of a low-pressure microbubble (LPMB) scrubber, which facilitates the determination of operational conditions of the scrubber via flow-pattern analysis. The LPMB scrubber maximizes the interfacial area of two-phase systems using the bubbly flow. Microbubbles have received attention due to their microscopic sizes, high residence time, and high mass-transfer efficiency. The LPMB scrubber maintains a negative outlet pressure to generate gas flow, which in turn generates microbubbles interrupting gas flow with three blocking plates in the atomizer. This gas flow generates a bubbly flux with different bubble sizes. To obtain bubble characteristics, we analyzed 20 atomizer images where this complex flux occurs. Bubble size, number of bubbles, gas void fraction, and IAC were calculated using an Open-CV Python algorithm. To validate the most appropriate bubble flow patterns, case studies were conducted at pressure difference of 240, 360, and 450 mmAq. The 360 mmAq condition had the lowest percentage of bubbles smaller than 50 μm, but the total number of bubbles, void fraction, and IAC were the highest. The results obtained in this study confirm that using an LPMB scrubber in an oxidizing solution facilitates reductions of 92.6, 93.9, and 99.9% in NO_X, SO_X, and dust, respectively. These results could be used to validate the bubble reactivity of other two-phase systems intended for commercial and practical applications.

Keywords: air pollutant removal, image processing, interfacial-area concentration, low-pressure microbubble, two-phase flow

1. Introduction

Microbubble technology is widely used in industrial applications, such as water treatment (Agarwal et al., 2011; Khuntia et al., 2012), bioreactors (AL-Mashhadani et al., 2015), polymers (Yap et al., 2014), petroleum plants (Telmadarreie et al., 2016), healthcare (Hernot and Klibanov, 2008), and chemical purification (Etchepare et al., 2017), because of the high mixing and mass-transfer efficiencies of the microbubble reactions. Furthermore, microbubbles have become the preferred choice for several industrial applications because of their peculiar characteristics of large gas-liquid interface areas (Zhang et al., 2015), high residence time in liquids (Hernandez-Alvarado et al., 2017), and high mass-transfer efficiency in gaseous and liquid phases (Muroyama et al., 2013).

Various researchers have attempted to demonstrate the characteristics of the bubble flow field. For example, Takahashi et al. (2007) studied the production of free radicals when the microbubbles collapse. AL-Mashhadani et al. (2015) obser-

ved microbubbles in a bubble reactor and verified their characteristics using computational fluid dynamics. In addition, the mass transfer performance of microbubbles was investigated by Takahashi (2005). Some researchers have investigated bubble effects for measuring parameters in stirring vessels (Laakkonen et al., 2005) or measuring the interfacial area in a bubble column (Maceiras et al., 2010), whereas others mainly employed probe-based or image-processing methods to identify these characteristics (Zhao et al., 2005).

It is well known that two-phase systems dominated by microbubbles possess higher interfacial areas, mass-transfer coefficients, and residence time than those dominated by large bubbles. In such a system, simultaneously identifying the size of the bubbles and their flow patterns is important. Therefore, many studies have used bubble columns to investigate the bubble effect. Columns have simple structures, thus enabling easy investigation of bubble sizes and pattern analysis. By interpreting these flow patterns, we can identify the desired bubble generation conditions. Pohorecki et al. (2001) performed experiments under various conditions with high temperatures and pressures in a bubble column. Mandal et al. (2005) measured gas holdup, bubble size distribution (BSD), and interfacial-area concentration (IAC) in bubble columns. Similarly, numerous studies on bubble generating methods have been published. Some authors have reported the performance of specific bubble generators. For example, Sadatomi et al. (2005) created a new microbubble

generator with a spherical body in a tube-type device and confirmed its performance. Meanwhile, Gordiychuk et al. (2016) determined the operational conditions for a Venturi-type bubble generator by confirming various parameters. Kim et al. (2017) investigated the effects of a swirling chamber and breaker disk in a pressurized-dissolution-type microbubble generator. In addition, Kim et al. (2018) optimized an ejector-type microbubble generator by adjusting the breaker disk distance. Furthermore, the generation method that uses a breaker disk is very similar to the system introduced in this study.

We are losing quality of life because of the recent continuous atmospheric pollution. Many studies have pointed out air pollutants such as NO_X, SO_X, and fine dust. Thus, a legal system is being established to reduce air pollutants worldwide, and research on air pollutants should be carried out in various ways. We determined the operating conditions of the low-pressure microbubble (LPMB) scrubber using image processing to meet and exceed air pollutant emission standards. Although microbubbles are used in various industries, little research on their use in air pollutant removal exists. Conventional methods for removing pollutants primarily involve wet scrubbing using a low-efficiency water spray (Ashtari et al., 2016). Moreover, the conventional bubble generation method is by using compressed gas injection (Fujiwara et al., 2003), which results in significant energy loss and increased risk of system corrosion (Kim et al., 2011). However, the developed LPMB scrubber can be operated under low-pressure conditions using only a suction blower. It is more economical than the compression method because compressed air is generally one of the most expensive utilities in industrial facilities (Dindorf, 2012). This LPMB scrubber is a new technology; therefore, to use it commercially, its effectiveness needs to be verified. In fact, this LPMB scrubber has already been used to dramatically remove air pollutants in commercial factories. However, the removal efficiency was unstable as it depended on the operational conditions, and the removal efficiency stability is necessary to meet government emissions standards. Therefore, we conducted a study to address this concern by maximizing the bubble effects. In this study, we developed a method for determining the optimal operating conditions of the industrial scale microbubble scrubber. In previous studies, researchers have measured the volume of flow fields by adjusting the flow field size and determining the bub-

ble size and IAC only in lab-scale bubble systems. However, in the industrial-scale microbubble scrubber, calculating the IAC by conventional methods is impossible because the observation flow field is too large for defining the flow field volume with ease. In this work, we developed a method for calculating IAC in real-time by determining the flow field volume with a three-dimensional concept using the camera focal distance and derived optimal operating conditions of the LPMB scrubber (Figure 1).

Accordingly, in this study, we investigated the principle of bubble formation in an LPMB scrubber used in industrial applications and developed a model for determining its operational conditions through immediate IAC comparisons. In Section 2, we introduce the principles of the LPMB scrubber, experimental conditions, and method of measuring IAC. Section 3 presents the results of specific experiments and the appropriate operational conditions of the LPMB scrubber through IAC comparisons. Section 4 summarizes the results and presents our main conclusions.

2. Materials and Methods

2.1. Actual Process Conditions

The LPMB system consists of four scrubbing stages, as shown in Figure 2(a). The scrubber in each stage is connected in series with the others, and the role of each stage is slightly different. The first stage is responsible for the cooling of the gas and adsorption of dust. In the second stage, the adsorption of the remaining dust and oxidation of NO using oxidants are achieved. Previous studies have shown that the proper adjustment of pH is essential for both adsorption and absorption (Zhao et al., 2019). Therefore, when pH increased, it was adjusted by injecting sulfuric acid in the second stage. The third stage involves dissolving SO_X using NaOH and oxidizing the remaining NO. The final stage involves dissolving NO_X and any remaining SO_X. Each scrubber has one gas suction blower with a capacity of 10 Nm^3/min and a maximum pressure difference (ΔP) of 550 mmAq. The scrubber was operated at ΔP values of 240, 360, and 450 mmAq. Additionally, the third scrubber was investigated mainly because it is primarily responsible for oxidizing NO. Therefore, we investigated the generation of bubbles at different ΔP values to analyze the gas-oxidation effect.
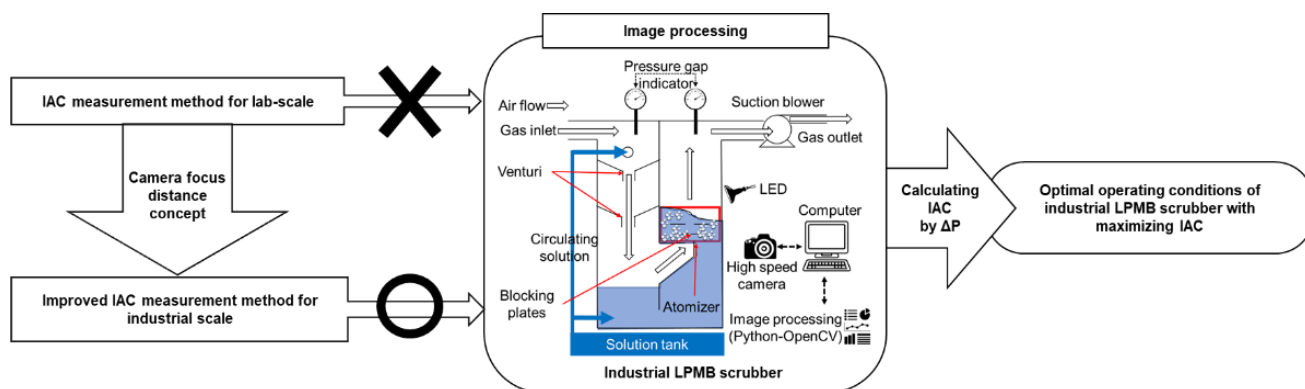

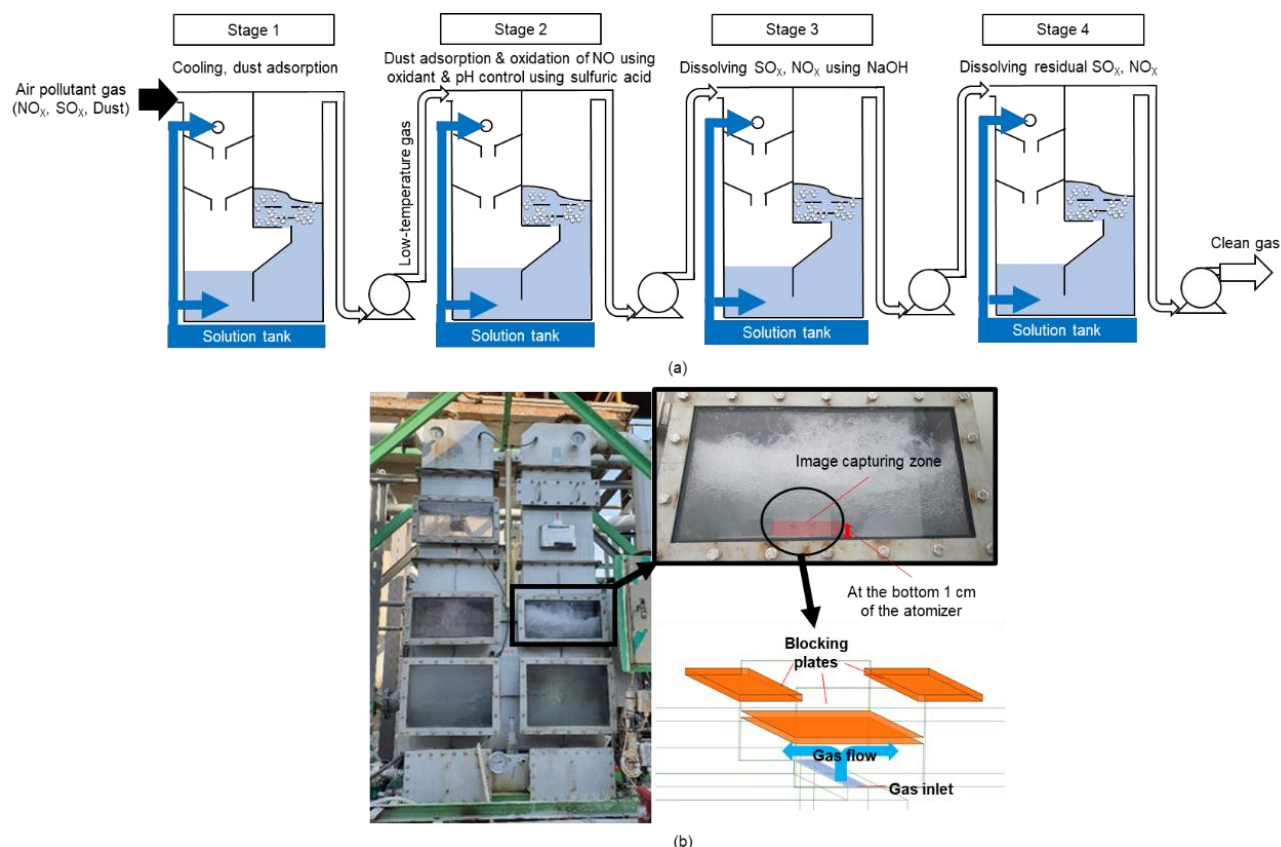**Figure 1.** Summary of the overall research.

Figure 2. Overview of the low-pressure microbubble (LPMB) scrubber; (a) Schematic of the LPMB scrubber system used industrially and (b) LPMB scrubber and atomizer.
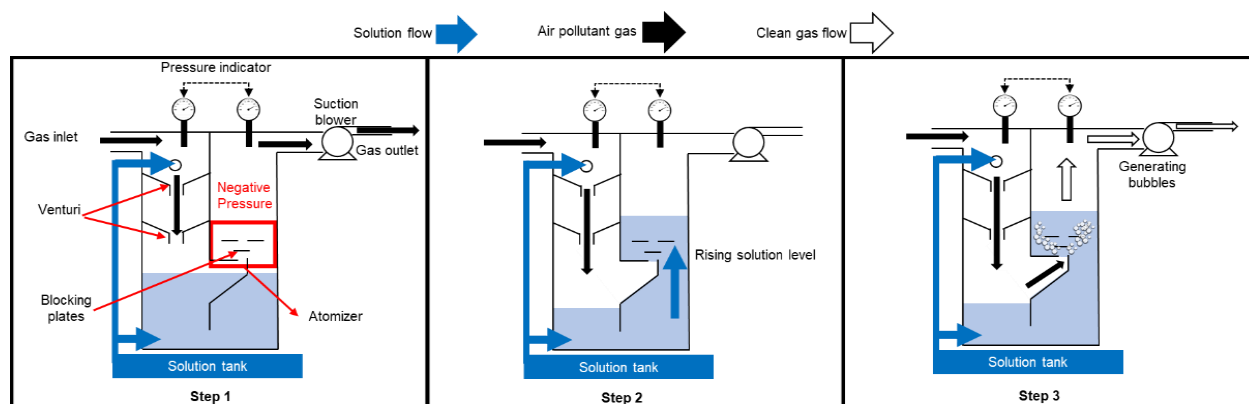

Figure 3. Operating sequence of the LPMB scrubber.

This scrubber generates microbubbles in three steps. First, the inside of the scrubber is filled with an oxidizing solution below the atomizer, and negative pressure is maintained at the outlet using a suction blower. Second, ΔP changes the solution level in the scrubber, and the solution level rises to the height of the blocking plates. In the last step, the rising gas flow and blocking plates generate microbubbles as a complex bubbly flow (Figure 2(b)). These blocking plates interrupt the gas flow and break the rising large bubbles. The sequence of the scrubber operation is presented in Figure 3.

In the experiment, a company, whose name is not mentioned owing to privacy issues, used this LPMB scrubber to self-produce oxidizing solutions for removing fine dust-causing substances. This is a well-known method of oxidizing NO to NO_2 and dissolving NO_X (Sun et al., 2020). NO_2 is more soluble than NO when oxidized. The oxidizing solution was mainly used in the second, third, and fourth scrubbers. In addition, "Testo 350k" and "Vario Plus Industrial" were used to measure the efficiency. The removal efficiencies of NO_X, SO_X, and dust were measured to be over 90%.

2.2. Analysis of Microbubble Characteristics Using Image Processing

2.2.1. Conditions for Capturing Images

The inside of the atomizer has bubbles of different sizes in the flow. Microbubbles are distributed at a lower position in the atomizer than large bubbles because of their small size (Figure 4). Therefore, an image of the bottom 1 cm of the atomizer was captured to observe the features of the microbubbles. In addition, a Sony A7m3 DSLR camera and a Laowa 24 mm f/14 Probe lens were used to capture bubble images. The Laowa lens is an LED-light-embedded lens that can easily capture tiny structures. During experiments, microbubbles are generally observed by placing an additional light source on the opposite side (Burns et al., 1997; Yin et al., 2015; Prakash et al., 2020). Observation is easy in such environments because of the shadows cast on the bubbles. However, in our case, image extraction was performed in an actual industrial environment; consequently, it was difficult to set the LED light on the opposite side. Therefore, we created a bright environment by placing a lens-LED light at the camera position.

Figure 4. Bubble-image extraction in the atomizer using a DSLR camera.

2.2.2. Method for IAC Measurement

After the images were captured, image processing was performed to determine several factors. We mainly used Open-CV Python for image processing (Bradski, 2000). Python programming was extensively used in this study because of the availability of several ready-to-use libraries for working with images and the ease of code adaptability to other programs (Ivanov et al., 2019). Open-CV is a programming library commonly used for image processing that can be imported from Python (Yang et al., 2018).

Almost all images contain image distortion errors because of the physical lens properties of circular structures (Choi et al., 2006). In industries that use images, research is being conducted on image correction to minimize such errors. However, in this experiment, we overcame this problem by excluding areas where image distortion errors appeared. Therefore, the image-processing detection range was set to the center portion (1,000 × 1,000 pixels) of the image that was less distorted, as shown in Figure 5.
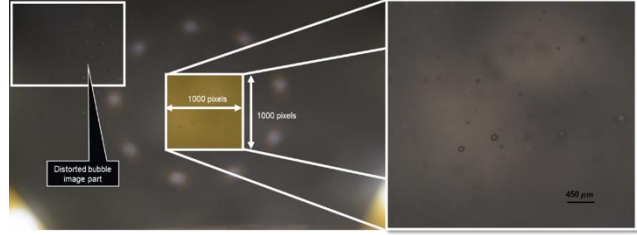

Figure 5. Condition setting for bubble size measurement.

The bubble detection algorithm includes four steps and was designed based on the research by Ivanov et al. (2019). The first step is Gaussian blur, and the second step is Canny edge detection (Canny, 1986). The third step involves making contours, and the final step is the process of extracting data. The first step in image processing is to apply gray scale and Gaussian blur to the image before applying the edge detection code (Figure 6(b)). Generally, this is done before Canny edge detection because it dramatically reduces the noise in the original image. The second step uses Canny edge detection (Figure 6 (c)). This step involves searching for the edge and finding the vertical line perpendicular to the gradient line. The third step is morphological transformation. This step identifies the shape by separating the contours and simplifying, as shown in Figure 6 (d). The final step is image data extraction. Before extraction, it is assumed that the microbubbles are spherical. Then, the Python algorithm can easily measure the size of the bubble contour by drawing a circle. The radius and center are specified based on the bubble contour size and position. The acquired radius data are defaulted based on the number of pixels. Therefore, representative images are required to measure the actual distance per pixel. This value is obtained by taking images at a sharp edge distance. Figure 4 shows an image taken at a sharp edge distance. In addition, the total number of bubbles and average bubble length were printed on the image to facilitate data extraction (Figure 7). The data were extracted using the Python code, and the bubble data were rearranged using another program. In previous studies, researchers mainly focused on image processing to extract and analyze bubble size data (Gaillard et al., 2015). In our study, however, we present a methodology to calculate IAC using the camera focal distance that can be determined from a particular bubble flow field.

IAC is one of the most important parameters for confirming the effect of active interfaces. In multiphase flow systems, high interface areas have many advantages because there are many opportunities for the two phases to interact with each other. In addition, research on the bubble column was conducted by comparing the IAC measured here with that reported in previous studies (Mandal et al., 2005). Therefore, comparing IACs is crucial for validating the effects of physical characteristics. Generally, the IAC depends on the SMD and gas void fraction. Therefore, the IAC value was calculated using Equation (1) given by Nedeltchev et al. (2006):

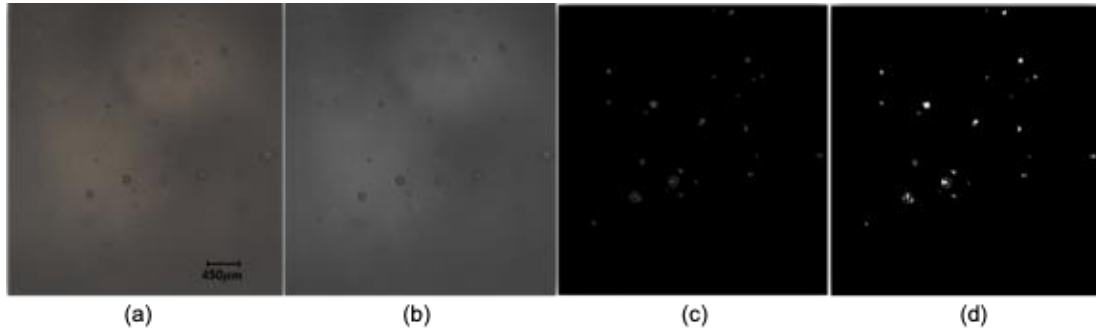$$IAC = \frac{6\phi_{gas}}{d_{32}} \tag{1}$$

Figure 6. Image-processing algorithm workflow for bubble-size measurement; (a) original image, (b) after Gaussian blur, (c) Canny-edge detection, and (d) morphological transformation.

where ϕ_{gas} is the gas void fraction in the flow field, and d_{32} is the SMD. The ϕ_{gas}, which contains volume information, should be determined to calculate the IAC based on Equation (1). Therefore, a simple experiment was conducted to calculate the gas void fraction, as shown in Figure 8.
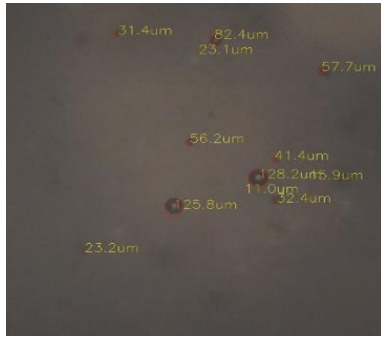

Figure 7. Sample image-processing results for bubble-size measurement.

To measure the distance detectable by the camera, a method of measuring the distance from the photographic sharpness was considered (Murawski, 2015). First, the flow field volume was determined by measuring the focus depth distance of the camera. This was an experiment that determined the correlation of the volume information regarding the bubble image. The images were captured by adjusting the distance between the camera and bubbles. When the edges of the bubbles are ambiguous, the filming distance is called the maximum detectable distance and minimum detectable distance. The volume in which the camera can observe bubbles is the camera detectable volume (V_{cd}), which can be defined as follows:

$$V_{cd} = D_{cd} A_{ip} \qquad (2)$$

In Equation (2), A_{ip} is the image-processing detection range described earlier, and D_{cd} is the distance between the bubbles that can be detected by the edge and camera lens. Therefore, ϕ_{gas} can be calculated as follows:

$$\phi_{gas} = \frac{V_{tb}}{V_{cd}} \qquad (3)$$

where V_{tb} is the total bubble volume of the flow field. Additionally, V_{tb} can be determined through the data for each bubble volume extracted via image processing.
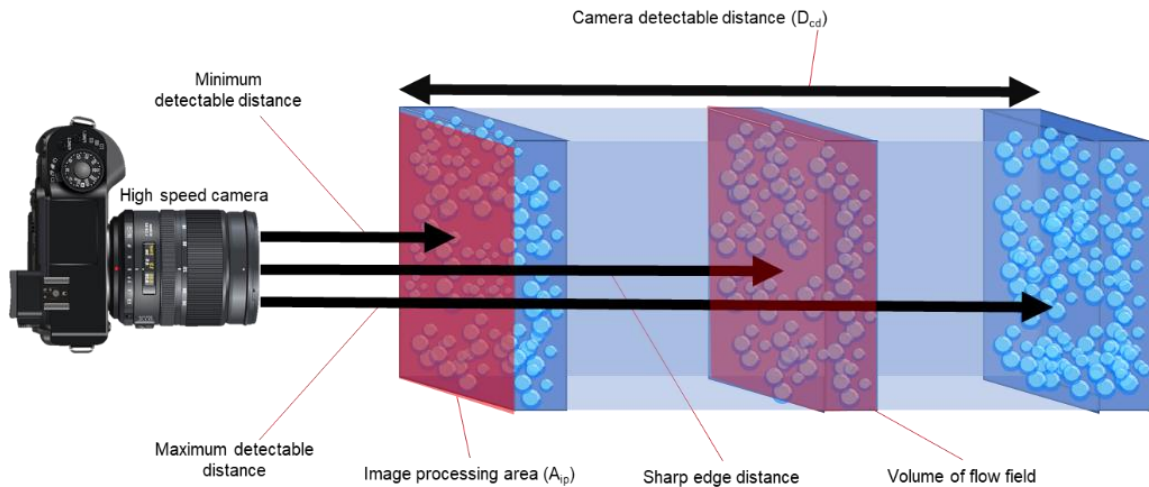

Figure 8. Schematic of the experiment to measure the volume of bubble flow field.
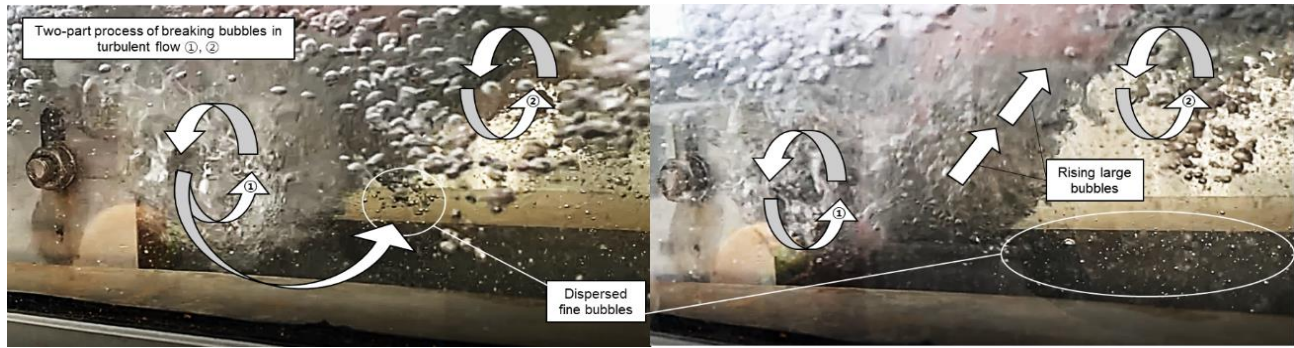
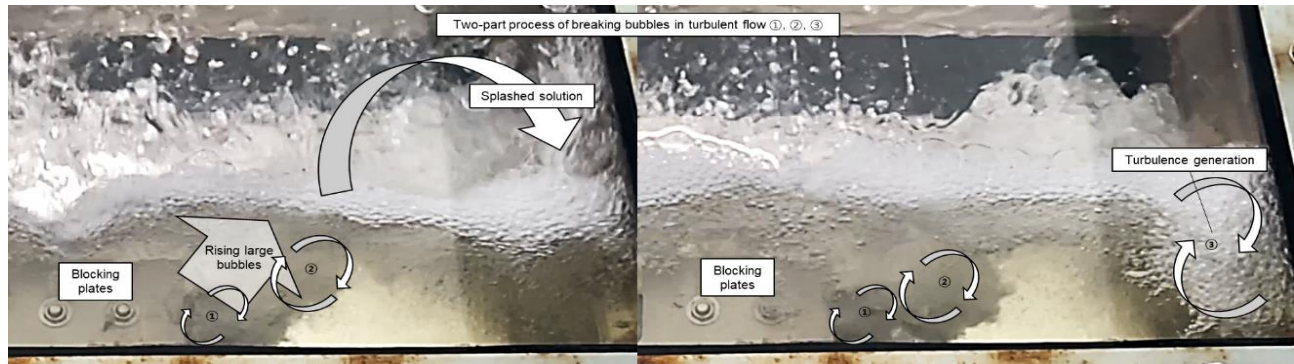**Figure 9.** Two-part bubble-breaking process by blocking plates.

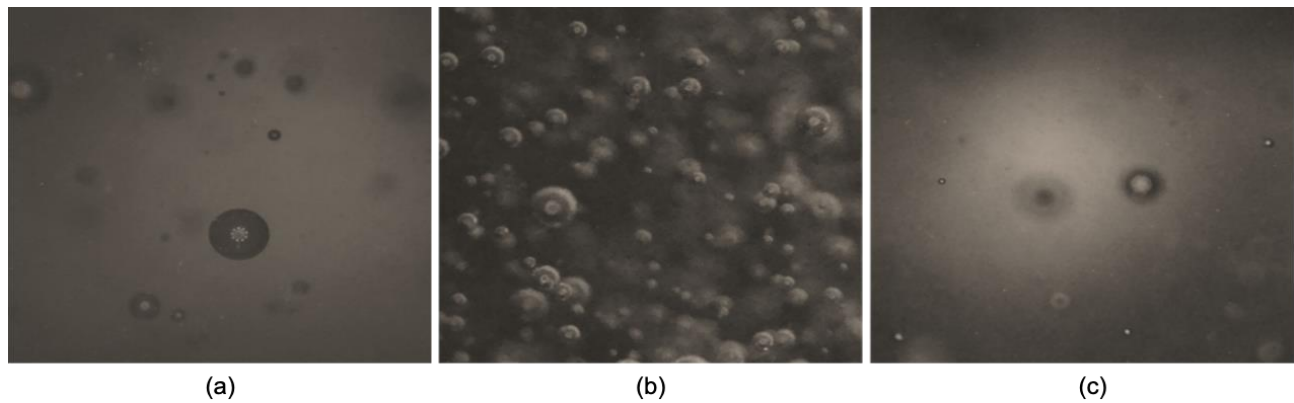**Figure 10.** Bubble-breaking process at the gas-liquid interface.

Figure 11. Sample bubble images captured using a DSLR camera with a macro lens at ΔP of (a) 240, (b) 360, and (c) 450 mmAq.
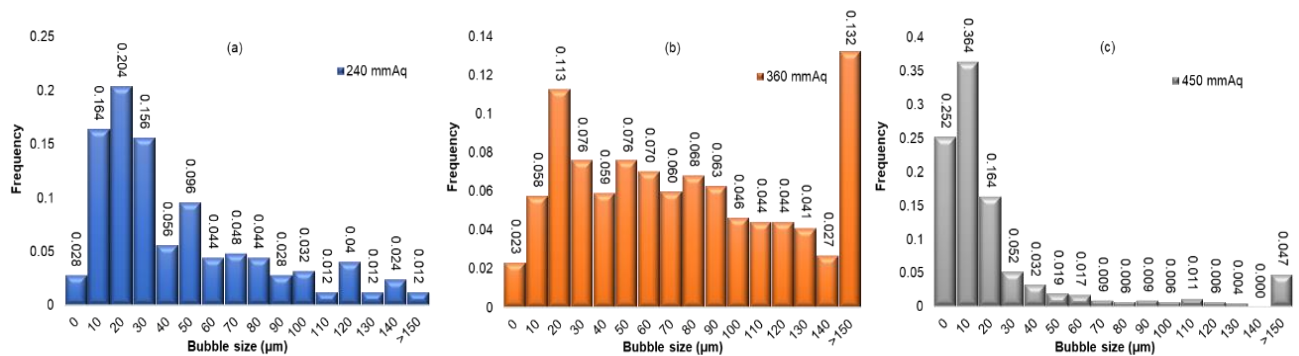

Figure 12. Bubble-size distributions in atomizer for ΔP of (a) 240, (b) 360, and (c) 450 mmAq.

3. Results and Discussion

3.1. Bubble Generating Process in Atomizer

The LPMB scrubber generates bubbles mainly by interrupting gas flow with blocking plates. However, the bubble formation process occurs too quickly to be observed using a conventional camera. Therefore, a DSLR camera was used to monitor the bubble-breaking mechanism from the blocking plates. Figure 9 shows that the breaking bubbles are dispersed into the turbulent flow generated by the blocking plates (Chu et al., 2019). As shown in Figure 9, ① occurs when the turbulent flow interacts with the first blocking plate, and ② represents the second turbulent flow section that is caused by the two blocking plates placed over the first blocking plate.

Bubbles are also formed at the two-phase interface. In other words, the flow of large bubbles creates solution waves and forms turbulence by interacting with the wall. This process is shown in Figure 10. Therefore, the bubble formation mechanism of the atomizer can be seen in three parts. In the first part, fine bubbles are formed by turbulent flow near the blocking plates. The fine bubbles generated in this process are dispersed, but the remaining large bubbles rise. Second, bubbles are generated by turbulence at the point where they are far from the blocking plates. Third, rising large gas voids splash the solution liquid, which causes more turbulence at the edge of the atomizer. The three turbulent sections create a dominant bubbly flow field.

3.2. Analysis of BSD Based on ΔP

Twenty images were taken in the image-capturing zone with different ΔP conditions (Figure 2). An example of bubble image is shown in Figure 11. The number of bubbles observed in the images differs slightly.

The BSD was calculated based on the obtained data and is determined as shown in Figure 12. When ΔP was 240 mmAq, the frequency of the bubbles was concentrated in the range of 10 ~ 40 µm. The sum of the proportions in this range was more than 50%. The most dominant bubble in the range of 20 ~ 30 µm was slightly larger than that of the 450 mmAq condition because of the relatively low flow rate from the atomizer inlet. It seems that this led to a weak turbulence and a low dispersion of bubbles. However, under a ΔP of 360 mmAq, the BSD was evenly distributed. Bubbles larger than 100 µm accounted for more than 33% of the total number of bubbles. The proper location with blocking plates and solution level made it easier to form turbulence, and the large bubbles could stay in the liquid for a long time. At a ΔP of 450 mmAq, the bubble frequency between 10 and 20 µm was the highest, and the BSD exhibited a right-skewed distribution. This demonstrated that at 450 mm Aq, the fine bubble selectivity was higher than under other conditions. The high inlet gas flow rate of the atomizer led to gas turbulence and microbubble dispersion. However, the highly formed solution level led to a lack of interaction with the blocking plates. This interaction mainly caused large bubbles; hence, only microbubbles that could stay for a long time existed selectively (Loisy and Naso, 2017).

Figure 13 shows the number of microbubbles generated for each ΔP condition and the bubble ratio of less than 50 µm that had clear microbubble characteristics (Muroyama et al., 2013). Information on the number of bubbles was extracted from 20 images. The largest number of microbubbles was observed when ΔP was 360 mmAq. The results show that an increase in ΔP was not completely proportional to the number of bubbles. This is because a high ΔP causes a high solution level from the blocking plates of the atomizer. This high solution level reduces the interaction of the gas-liquid interface flux with the blocking plates. This results in a difference of approximately 50 mm in solution level for each ΔP, and it seems to maintain the appropriate solution level. Figure 13 shows the ratio below 50 µm and the total number of bubbles observed in 20 images under a difference in ΔP. Even though the ratio of bubbles below 50 µm is the lowest in 360 mmAq, the actual number of bubbles is the highest in the same condition because many bubbles have been produced. Microbubbles can maintain a uniform distribution within the flow field for a long time if they are smaller than 50 µm. Therefore, a uniform micro-bubble distribution can be determined under this condition.
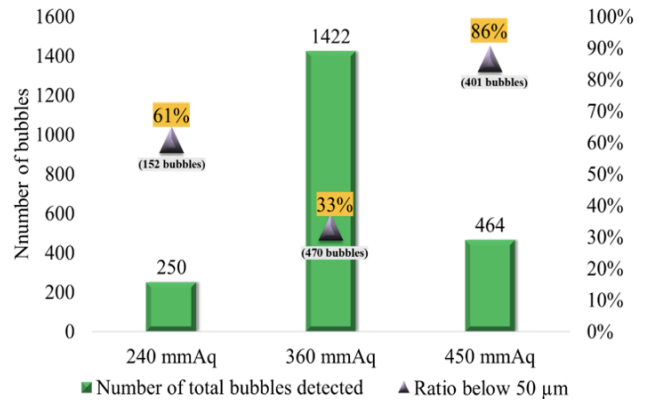

Figure 13. Number and percentage of bubbles measuring less than 50 µm for different ΔP values.

3.3. Comparison between the SMDs of Bubbles

The sizes of the bubbles in multiphase flux are estimated by measuring a single mean bubble diameter, which is called the volume-surface mean diameter (Kowalczuk and Drzymala, 2016), d_{32}, or the SMD. The SMD is calculated using Equation (4) (Prakash et al., 2018):

$$d_{32} = \frac{\sum_{i=1}^{n} n_i d_i^3}{\sum_{i=1}^{n} n_i d_i^2} \tag{4}$$

where d_i is the diameter of the bubble, and n_i is the number of each bubble, assuming the microbubbles have a spherical shape. The bubbles were assumed spherical because Equation (4) was derived by assuming a completely spherical shape in the SMD calculation process. In addition, the SMD is required to determine the IAC. The SMD and IAC are inversely proportional, as demonstrated by Equation (1).

The SMD pattern is shown in Figure 14(a). It tends to increase with ΔP. SMD was the largest at 450 mmAq because it was affected by the occasional presence of large bubbles. It is assumed that this proportional pattern is due to the large ΔP flow rate of gas, which results in complex turbulence and increases the residence time of large bubbles.

3.4. Comparison of Gas Void Fraction and IAC

The IAC was obtained using Equations (1), (2), and (3). To utilize Equation (2), the camera detection distance was measured, and the results are shown in Figure 15. The images were captured by adjusting the distance to 0.5 mm. D_{cd} was determined by finding a blurry point that was out of focus. The maximum and minimum detectable distances are the maximum and minimum distances from and till which the bubble border is clearly visible, respectively. The following results were determined using a camera detectable distance of approximately 1 mm. Additionally, A_{ip} was determined to be 9×10^{-6} m² because a bubble was detected based on $1,000 \times 1,000$ pixels. Finally, V_{cd} was calculated as 9×10^{-9} m³ based on Equation (2). Then, the void fraction was calculated using Equation (3), and the results are shown in Figure 14(b). This result is the average void fraction of the 20 images. Generally, the number of bubbles and void fraction are not proportional. This is because a high number of bubbles does not always indicate a high volume of bubbles. However, there was a relatively large difference in the number of bubbles; therefore, there was also a large difference in the void fraction. In addition, the void fraction tends to increase when relatively large bubbles are included. There-

fore, the highest void fraction was observed under 360 mmAq.

The calculated average IAC values at different values of ΔP in the LPMB scrubber are shown in Figure 14(c). The IAC at ΔP 360 mmAq was more than eight times that obtained at other ΔP (i.e., 240 and 450 mmAq) values. According to Equation (3), the void fraction and SMD are the factors that affect the IAC. However, the SMD did not have a significant impact on the results. Therefore, the IAC is determined by the void fraction within this LPMB scrubber. Figure 13 demonstrates a similar trend in the number of bubbles as seen for the IAC in Figure 14(c). This trend results from the dominance of the number of bubbles in the fluid field compared with other conditions.

By combining these results, it can be seen that the solution level difference with the blocking plates affects the formation of bubbles. Although it is difficult to determine a clear level in the bubble flow, it can be determined indirectly by ΔP. Therefore, the widest surfactant area was obtained at a ΔP of 360 mm Aq, which can maximize the efficiency of the oxidizing solution.

3.5. Identification of NO$_X$, SO$_X$, and Dust-Removal Efficiency in LPMB Scrubbers

The concentration of air pollutants was measured at Korea Testing Laboratory (KTL) and Korea Testing & Research Institute (KTR), which are authorized testing agencies in Korea. The efficiency of air pollutant removal was confirmed at a ΔP of 360 mmAq. The removal results measured the concentrations of NO$_X$, SO$_X$, and dust in the final discharge pipe. In the final discharge pipe, a gas passes through the LPMB scrubber
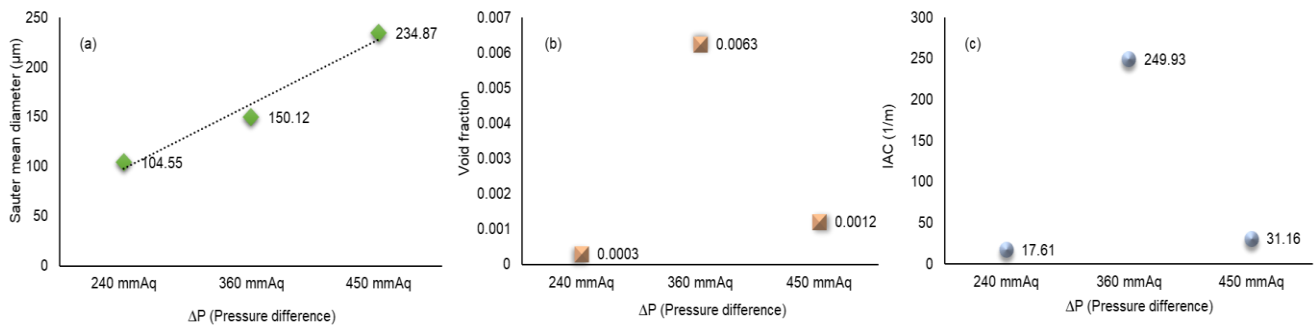

Figure 14. Comparison between (a) Sauter mean diameters, (b) void fractions, and (c) interfacial-area concentrations for different ΔP values.
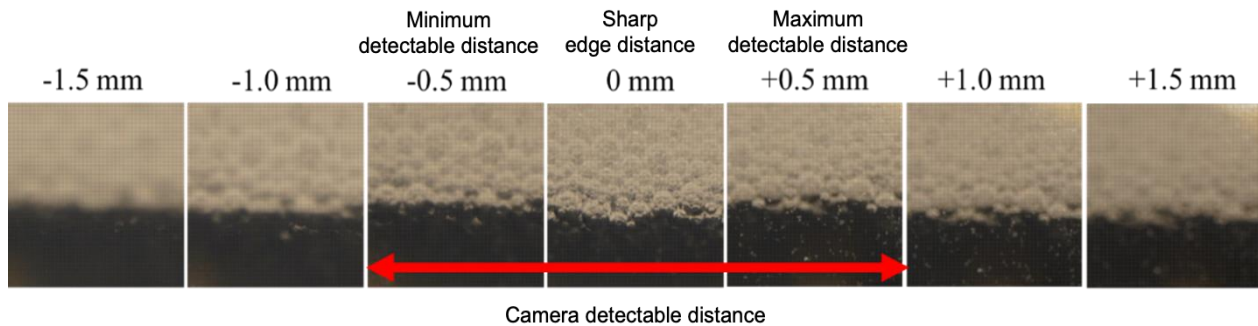

Figure 15. Photographic results used for determining the camera detectable distance.

after being discharged from limestone-fired furnaces. The measurement results are listed in Table 1. In addition, based on the Atmospheric Environmental Conservation Act, the pollutant-emission levels allowed by the Korean Government are less than 60 and 100 ppm for NO_X and SO_X, respectively, and less than 30 mg/Sm^3 for fine dust. As a result, when this LPMB scrubber was used, the emission standards could be met.

Table 1. NO_X, SO_X, and Dust-removal Efficiency of LPMB Scrubber under a ΔP of 360 mmAq

		KLT	KTR	Removal efficiency
Dust	Inlet	944.6 mg/Sm^3	none	99.9% (KTL)
	Outlet	0.5 mg/Sm^3	none	
NO_X	Inlet	90.5 ppm	124.5 ppm	92.6% (KTL)
	Outlet	6.7 ppm	35.0 ppm	71.9% (KTR)
SO_X	Inlet	none	16.5 ppm	93.9% (KTR)
	Outlet	none	< 1 ppm	

In this study, we determined the appropriate operational ΔP conditions by observing the bubble formation process of the LPMB scrubber and measuring the bubble size using image processing. It was confirmed that turbulence formed in the three parts of the atomizer, and the dispersion of the microbubbles was also investigated. The LPMB scrubber in which the IAC was the highest had a ΔP of 360 mmAq. In addition, the air pollutant removal efficiency under a ΔP of 360 mmAq was greater than 90%. The LPMB scrubber removes air pollutants by dissolving them; hence, a high air pollutant removal efficiency suggests a high mass transfer efficiency (Cho and Choi, 2019). It seems that the measured pollutant removal efficiency was high because of the high IAC value related to mass transfer efficiency.

4. Conclusions

In this study, the bubble generation mechanism of an LPMB scrubber and the bubble generation pattern corresponding to different ΔP values were analyzed using image processing. The LPMB scrubber is a system that uses a suction blower to form a gas flow and generates bubbles in the atomizer containing the blocking plates. Fine bubbles formed by interrupting the gas flow with blocking plates could be easily dispersed in the scrubber, and they were widely distributed below the atomizer. We extracted 20 images at each ΔP (i.e., 240, 360, and 450 mmAq) conditions and observed the bubble flow inside the LPMB scrubber. Python Open-CV functions were used for image processing, and the bubble size was measured using a Python algorithm. We calculated SMD and gas void fraction values from the bubble size data and finally determined the IAC using Equations (1), (2), (3), and (4). The SMD tended to increase with ΔP. At a ΔP of 360 mmAq, the ratio of bubbles less than 50 μm was the lowest, and the gas void fraction was calculated to be the highest. Another feature was that the BSD at this ΔP (i.e., 360 mmAq) had a more evenly spread BSD shape than that at other conditions and also had the highest number of bubbles. In addition, a high ΔP led to an increased

solution level difference of the LPMB scrubber. These results had a significant effect on the generation of bubbles at the appropriate height of the solution and the location of the blocking plates. Therefore, we observe that the IAC was more than eight times higher at 360 mmAq than under other conditions. NO_X, SO_X, and dust removal efficiencies were measured at this condition of the highest IAC. Removal efficiencies for dust, NO_X, and SO_X were measured as 99.9, 92.6, and 93.9%. Consequently, this scrubber met the pollutant-emission standards prescribed by the government.

In this study, we were able to identify the tendency of the IAC according to difference of ΔP in the LPMB scrubber. This result is expected to increase the operational efficiency of a process if ΔP with the highest IAC is maintained. It is also expected that further research on detailed operational conditions, including a case study on the effect of different inlet sizes of the atomizer and the initial capacity of the solution, will increase the efficiency of the LPMB scrubber.

References

Agarwal, A., Ng, W.J. and Liu, Y. (2011). Principle and applications of microbubble and nanobubble technology for water treatment. *Chemosphere*, 84(9), 1175-1180. https://doi.org/10.1016/j.chemosphere.2011.05.054

AL-Mashhadani, M.K.H., Wilkinson, S.J. and Zimmerman, W.B. (2015). Airlift bioreactor for biological applications with microbubble mediated transport processes. *Chem. Eng. Sci.*, 137, 243-253. https://doi.org/10.1016/j.ces.2015.06.032

Ashtari, A.K., Majd, A.M.S., Riskowski, G.L., Mukhtar, S. and Zhao, L. (2016). Removing ammonia from air with a constant pH, slightly acidic water spray wet scrubber using recycled scrubbing solution. *Front. Environ. Sci. Eng.*, 10, 1-10. https://doi.org/10.1007/s11783-016-0869-3

Bradski, G. (2000). The opencv library. *Dr Dobb's J. Softw., Tools*, 25, 120-125.

Burns, S.E., Yiacoumi, S. and Tsouris, C. (1997). Microbubble generation for environmental and industrial separations. *Sep. Purif. Technol.*, 11, 221-232. https://doi.org/10.1016/S1383-5866(97)00024-5

Canny, J. (1986). A computational approach to edge detection. *IEEE Trans. Pattern Anal. Mach. Intell.*, PAMI-8, 679-698. https://doi.org/10.1109/TPAMI.1986.4767851

Cho, H.J. and Choi, J. (2019). Calculation of the mass transfer coefficient for the dissolution of multiple carbon dioxide bubbles in sea water under varying conditions. *J. Marine Sci. Eng.*, 7(12), 457. https://doi.org/10.3390/jmse7120457

Choi, K.S., Lam, E.Y. and Wong, K.K.Y. (2006). Automatic source camera identification using the intrinsic lens radial distortion. *Opt. Express.*, 14, 11551-11565. https://doi.org/10.1364/oe.14.011551

Chu, P., Finch, J., Bournival, G., Ata, S., Hamlett, C. and Pugh, R.J. (2019). A review of bubble break-up. *Adv. Colloid Interface Sci.*, 270, 108-122. https://doi.org/10.1016/j.cis.2019.05.010

Dindorf, R. (2012). Estimating potential energy savings in compressed air systems. *Proc. Eng.*, 39, 204-211. https://doi.org/10.1016/j.pro-

eng.2012.07.026

Etchepare, R., Azevedo, A., Calgaroto, S. and Rubio, J. (2017). Removal of ferric hydroxide by flotation with micro and nanobubbles. *Sep. Purif. Technol*., 184, 347-353. https://doi.org/10.1016/j.seppur.2017.05.014

Fujiwara, A., Takagi, S., Watanabe, K. and Matsumoto, Y. (2003). Experimental study on the new micro-bubble generator and its application to water purification system. *ASME FEDSM*, 1 A, 469-473. https://doi.org/10.1115/fedsm2003-45162

Gaillard, T., Honorez, C., Jumeau, M., Elias, F. and Drenckhan, W. (2015). A simple technique for the automation of bubble size measurements. *Colloids Surf, A Physicochem. Eng. Asp*., 473, 68-74. https://doi.org/10.1016/j.colsurfa.2015.01.089

Gordiychuk, A., Svanera, M., Benini, S. and Poesio, P. (2016). Size distribution and Sauter mean diameter of micro bubbles for a Venturi type bubble generator. *Exp. Therm. Fluid Sci*., 70, 51-60. https://doi.org/10.1016/j.expthermflusci.2015.08.014

Hernandez-Alvarado, F., Kalaga, D.V., Turney, D., Banerjee, S., Joshi, J.B. and Kawaji, M. (2017). Void fraction, bubble size and interfacial area measurements in co-current downflow bubble column reactor with microbubble dispersion. *Chem. Eng. Sci*., 168, 403-413. https://doi.org/10.1016/j.ces.2017.05.006

Hernot, S. and Klibanov, A.L. (2008). Microbubbles in ultrasound-triggered drug and gene delivery. *Adv Drug Deliv. Rev*., 60, 1153-1166. https://doi.org/10.1016/j.addr.2008.03.005

Ivanov, M.V, Gavrilev, S.A., Tyurina, J.M., Yusipova, A. and Boldyrev, M.D. (2019). Developing photo analyzing and bubble processing program on Python language. *Lect. Notes Eng. Comput. Sci. Proc. World Congr. Eng. 2019*, London, U.K., 0958, 299-303.

Khuntia, S., Majumder, S.K. and Ghosh, P. (2012). Microbubble-aided water and wastewater purification: A review. *Rev. Chem. Eng.*, 28(4-6), 191-221. https://doi.org/10.1515/revce-2012-0007

Kim, H.S., Lim, J.Y., Park, S.Y. and Kim, J.H. (2018). Effects of distance of breaker disk on performance of ejector type microbubble generator. *KSCE J. Civ. Eng*., 22, 1096-1100. https://doi.org/10.1007/s12205-017-0208-7

Kim, H.S., Lim, J.Y., Park, S.Y. and Kim, J.H. (2017). Effects on swirling chamber and breaker disk in pressurized-dissolution type micro-bubble generator. *KSCE J. Civ. Eng*., 21, 1102-1106. https://doi.org/10.1007/s12205-016-1075-3

Kim, J., Lim, W., Lee, Y., Kim, S., Park, S.R., Suh, S.K. and Moon, I. (2011). Development of corrosion control document database system in crude distillation unit. *Ind. Eng. Chem. Res*., 50, 8272-8277. https://doi.org/10.1021/ie101871a

Kowalczuk, P.B. and Drzymala, J. (2016). Physical meaning of the Sauter mean diameter of spherical particulate matter. *Part. Sci. Technol*., 34, 645-647. https://doi.org/10.1080/02726351.2015.1099582

Laakkonen, M., Honkanen, M., Saarenrinne, P. and Aittamaa, J. (2005). Local bubble size distributions, gas-liquid interfacial areas and gas holdups in a stirred vessel with particle image velocimetry. *Chem. Eng. J*., 109, 37-47. https://doi.org/10.1016/cej.2005.03.002

Loisy, A. and Naso, A. (2017). Interaction between a large buoyant bubble and turbulence. *Phys. Rev. Fluids*., 2(1), 014606. https://doi.org/10.1103/PhysRevFluids.2.014606

Maceiras, R., Álvarez, E. and Cancela, M.A. (2010). Experimental interfacial area measurements in a bubble column. *Chem. Eng. J*., 163, 331-336. https://doi.org/10.1016/j.cej.2010.08.011

Mandal, A., Kundu, G. and Mukherjee, D. (2005). A comparative study of gas holdup, bubble size distribution and interfacial area in a downflow bubble column. *Chem. Eng. Res. Des*., 83, 423-428. https://doi.org/10.1205/cherd.04065

Murawski, K. (2015). Method of measuring the distance to an object based on one shot obtained from a motionless camera with a fixed-focus lens. *Acta Phys. Pol. A*, 127, 1591-1595. https://doi.org/10.12693/APhysPolA.127.1591

Muroyama, K., Imai, K., Oka, Y. and Hayashi, J. (2013). Mass transfer properties in a bubble column associated with micro-bubble dispersions. *Chem. Eng. Sci*., 100, 464-473. https://doi.org/10.1016/j.ces.2013.03.043

Nedeltchev, S., Jordan, U. and Schumpe, A. (2006). Correction of the penetration theory applied to the prediction of k_La in a bubble column with organic liquids. *Chem. Eng. Technol*., 29, 1113-1117. https://doi.org/10.1002/ceat.200600158

Pohorecki, R., Moniuk, W., Zdrójkowski, A. and Bielski, P. (2001). Hydrodynamics of a pilot plant bubble column under elevated temperature and pressure. *Chem. Eng. Sci*., 56, 1167-1174. https://doi.org/10.1016/S0009-2509(00)00336-5

Prakash, R., Kumar Majumder, S. and Singh, A. (2020). Bubble size distribution and specific bubble interfacial area in two–phase micro-structured dense bubbling bed. *Chem. Eng. Res. Des*., 156, 108-130. https://doi.org/10.1016/j.cherd.2020.01.032

Prakash, R., Majumder, S.K. and Singh, A. (2018). Flotation technique: Its mechanisms and design parameters. *Chem. Eng. Process. Process Intensif.*, 127, 249-270. https://doi.org/10.1016/j.cep.2018.03.029

Sadatomi, M., Kawahara, A., Kano, K. and Ohtomo, A. (2005). Performance of a new micro-bubble generator with a spherical body in a flowing water tube. *Exp. Therm. Fluid Sci*., 29, 615-623. https://doi.org/10.1016/j.expthermflusci.2004.08.006

Sun, H., Yang, G., Aftab, T. Bin, Xue, F., Xiao, Z., Guo, Q. and Li, D. (2020). Direct catalytic oxidation and removal of NO in flue gas by the micro bubbles gas–liquid dispersion system. *Int. J. Ind. Chem*., 11, 11-21. https://doi.org/10.1007/s40090-019-00198-6

Takahashi, M. (2005). Potential of microbubbles in aqueous solutions: Electrical properties of the gas–water interface. *J. Phys. Chem. B*, 109, 21858-21864. https://doi.org/10.1021/jp0445270

Takahashi, M., Chiba, K. and Li, P. (2007). Free-radical generation from collapsing microbubbles in the absence of a dynamic stimulus. *J. Phys. Chem. B*, 111, 1343-1347. https://doi.org/10.1021/jp0669254

Telmadarreie, A., Doda, A., Trivedi, J.J., Kuru, E. and Choi, P. (2016). CO_2 microbubbles – A potential fluid for enhanced oil recovery: Bulk and porous media studies. *J. Pet. Sci. Eng*., 138, 160-173. https://doi.org/10.1016/j.petrol.2015.10.035

Yang, J., Breault, R.W. and Rowan, S.L. (2018). Applying image processing methods to study hydrodynamic characteristics in a rectangular spouted bed. *Chem. Eng. Sci*., 188, 238-251. https://doi.org/10.1016/j.ces.2018.05.057

Yap, R.K.L., Whittaker, M., Diao, M., Stuetz, R.M., Jefferson, B., Bulmus, V., Peirson, W.L., Nguyen, A.V. and Henderson, R.K. (2014). Hydrophobically-associating cationic polymers as microbubble surface modifiers in dissolved air flotation for cyanobacteria cell separation. *Water Res*., 61, 253-262. https://doi.org/10.1016/j.watres.2014.05.032

Yin, J., Li, J., Li, H., Liu, W. and Wang, D. (2015). Experimental study on the bubble generation characteristics for an venturi type bubble generator. *Int. J. Heat Mass Transf*., 91, 218-224. https://doi.org/10.1016/j.ijheatmasstransfer.2015.05.076

Zhang, W.H., Zhang, J., Zhao, B. and Zhu, P. (2015). Microbubble size distribution measurement in a DAF system. *Ind. Eng. Chem. Res.*, 54, 5179-5183. https://doi.org/10.1021/acs.iecr.5b00109

Zhao, D., Guo, L., Lin, C. and Zhang, X. (2005). An experimental study on local interfacial area concentration using a double-sensor probe. *Int. J. Heat Mass Transf*., 48, 1926-1935. https://doi.org/10.1016/j.ijheatmasstransfer.2004.12.009

Zhao, S., Huang, W.W., Wang, X.Q., Fan, Y.R. and An, C.J. (2019). Sorption of Phenanthrene onto Diatomite under the influences of solution chemistry: a study of linear sorption based on maximal information coefficient, *J. Env. Inform*., 34(1), 35-44. https://doi.org/10.3808/jei.201600329